ACS APPLIED ENERGY MATERIALS

www.acsaem.org Article

Atomistic Insights into the Effects of Doping and Vacancy Clustering on Li-Ion Conduction in the Li_3OCl Antiperovskite Solid Electrolyte

Matt J. Clarke, James A. Dawson, Timothy J. Mays, and M. Saiful Islam*

Cite This: https://doi.org/10.1021/acsaem.1c00656 Read Online

ACCESS | Metrics & More | Article Recommendations | Supporting Information

ABSTRACT: Solid-state batteries are currently attracting increased attention because of their potential for significant improvements in energy density and safety as compared to liquid electrolyte-based batteries. Lithium-rich antiperovskites, such as Li_3OCl, are of particular interest, but the effects of doping on lithium mobility are not fully understood at the atomic level. Here, we investigate the impact of divalent cation (Mg^{2+}, Ca^{2+}, Sr^{2+}, and Ba^{2+}) and F^- doping on the ion conduction properties of Li_3OCl, using both defect simulation and molecular dynamics techniques. Our results show that the F-doped system has a low conductivity and high activation barriers. This is attributable to high binding energies, which leads to the formation of stable dopant−vacancy pairs, preventing long-range lithium-ion mobility. In contrast to the F-doped system, Mg dopants (shown to be the most favorable dopant on the Li^+ site) have lower binding energies to lithium vacancies, yielding higher lithium-ion conductivities and lower migration energies. Our results indicate a viable doping strategy to improve the electrochemical performance of antiperovskite solid electrolytes.

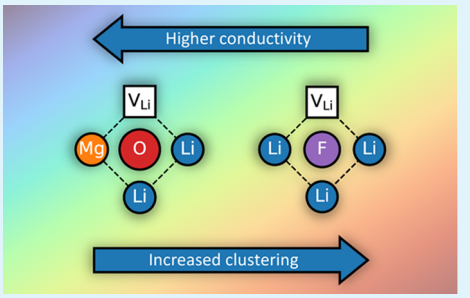

KEYWORDS: *antiperovskite, solid electrolyte, lithium battery, defects, doping, ion conduction*

INTRODUCTION

Solid electrolytes have attracted significant research in recent years due to the safety, stability, and energy density benefits, which solid-state batteries can provide over conventional liquid electrolyte systems.[1−15] In particular, solid electrolytes may enable the use of high-voltage electrodes or lithium−metal anodes, which are incompatible with current liquid electrolytes.[3−5,16] However, despite the potential benefits of solid electrolytes, transport issues at the electrode interface and the reduced ionic conductivity versus their liquid counterparts have thus far prevented their widespread adoption.[3,6,7,17,18]

Li-rich antiperovskites (Li_3OX with X = Cl or Br) are promising solid electrolyte candidates with good cyclability, high stability, wide electrochemical windows, and negligible electronic conductivity.[19−24] The perovskite structure is also highly amenable to chemical substitution and modification, allowing for the optimization of ionic conductivity or stability.[19,25,26] Early work by Zhao and Daemen[19] reported migration barriers as low as 0.2−0.3 eV and conductivities of 1.94×10^{-3} S cm^{-1} at room temperature. This compares favorably with mature systems such as the lithium lanthanum zirconium oxide garnet[27] at 2.06×10^{-3} S cm^{-1}. However, subsequent studies on Li_3OCl have indicated higher migration barriers (~0.6 eV) and lower conductivities.[28−33] A number of reasons for this discrepancy have been proposed, including the formation of hydroxide derivatives,[29,34−36] grain boundary effects,[37−39] and inadvertent cation doping during synthesis.[33] Issues surrounding the hygroscopic nature of antiperovskites and stability at high voltages are potential barriers to practical applications.[1,40]

In attempts to enhance their performance, a range of chemical modifications have been studied, including the mixing of mobile ions, doping, and the incorporation of polyanionic species.[19,31,41−48] Braga et al.[42,43] demonstrated that divalent doping (M = Mg^{2+}, Ca^{2+}, or Ba^{2+}) increased the Li-ion conductivity of Li_3OCl by an order of magnitude. Mg^{2+} doping is of particular interest as its small ionic radius limits lattice distortion, preventing glass formation at low temperatures.[44] Fluorine doping in the hydrated antiperovskite $Li_2(OH)X$ (X = Cl or Br) has been demonstrated to enhance ionic conductivity by Li et al.[31] but has not been considered in the context of Li_3OCl.

Despite the recent interest in lithium-rich antiperovskites, there is limited information on the fundamental atomistic factors that control their macroscopic dopant properties, which is valuable in facilitating targeted experimental work. An understanding of the interactions between mobile ions and dopant species over large timescales and length scales is key to overcoming known limiting factors, such as grain boundary resistance. Here, we address this shortcoming by studying the

Received: March 5, 2021
Accepted: April 6, 2021

https://doi.org/10.1021/acsaem.1c00656
ACS Appl. Energy Mater. XXXX, XXX, XXX−XXX

impact of divalent cation (Mg^{2+}, Ca^{2+}, Sr^{2+}, and Ba^{2+}) and F^- doping on the Li-ion transport properties of Li_3OCl. In particular, we consider the modes of dopant incorporation and the possibility of defect clustering from dopant−vacancy interactions in order to develop an atomistic understanding of the factors that may affect long-range lithium-ion conduction.

RESULTS AND DISCUSSION

Dopant Reactions and Li-Ion Conductivity. The Li_3OCl antiperovskite crystal structure consists of oxide ions at the typical B-site of an ABX_3 perovskite, coordinated to six Li^+ ions at the X-site and the large Cl^- ion occupying the 12-coordinate A-site, as shown in Figure 1a. The simulated lattice

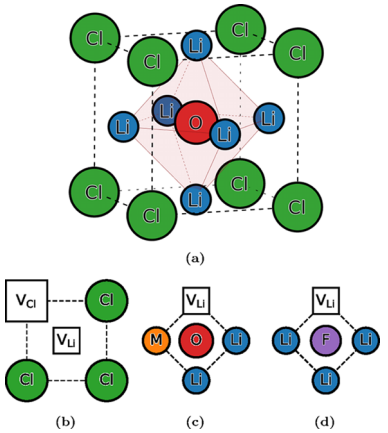

Figure 1. (a) Antiperovskite crystal structure of Li_3OCl and nearest-neighbor defect pair clusters for (b) LiCl Schottky defects, (c) M^{2+} doping, and (d) F^- doping in antiperovskite Li_3OCl. Li^+ ions are shown in blue, O^{2-} in red, Cl^- in green, F^- in purple, and M^{2+} in orange. Vacancies are indicated by black squares.

parameter for bulk Li_3OCl is 3.921 Å, with only a −0.36% difference to the observed diffraction value of 3.907 Å,[49] showing good reproduction of the experimental structure.

In terms of modes of dopant incorporation, cation dopants can substitute at the Li site, whereas anion dopants can sit at either O or Cl sites with the creation of charge-compensating defects where necessary. This raises key questions in relation to the favored substitution site, the type of compensating defect, and the influence (if any) of host ion size. Our simulation methods can probe these issues by generating quantitative estimates of the relative energies of different modes of dopant incorporation (sometimes termed modes of solution). Although the prediction of the precise amount of the dopant that can be incorporated is less straightforward, our results can provide a useful systematic guide to the site selectivity for different dopant species and to trends in dopant solubility. Such an approach has been applied successfully to a variety of perovskite oxide ionic conductors.[50−52]

We have therefore examined a range of dopants in Li_3OCl including divalent cations (Mg, Ca, Sr, and Ba) on the Li site and F^- on the O site. In order to form lithium vacancies, the following solution modes are viable:

M^{2+} on the Li^+ site is charge-compensated by V'_{Li}

$$MCl_2 + 2Li^{\times}_{Li} \rightarrow M^{\bullet}_{Li} + V'_{Li} + 2LiCl \quad (1)$$

F^- on the O^{2-} site is charge-compensated by V'_{Li}

$$LiF + Li^{\times}_{Li} + O^{\times}_{O} \rightarrow F^{\bullet}_{O} + V'_{Li} + Li_2O \quad (2)$$

where in the Kroger−Vink notation, $M^{\bullet}_{Li}$ and $F^{\bullet}_{O}$ signify M^{2+} and F^- dopant substitutional defects, respectively, with V'_{Li} signifying a Li^+ vacancy. However, the possibility of other favorable compensation mechanisms could prevent dopants from creating the desired lithium vacancies required for long-range diffusion:

M^{2+} on the Li^+ site is charge-compensated by Cl'_i

$$MCl_2 + Li^{\times}_{Li} \rightarrow M^{\bullet}_{Li} + Cl'_i + LiCl \quad (3)$$

F^- on the Cl^- site

$$LiF + Cl^{\times}_{Cl} \rightarrow F^{\times}_{Cl} + LiCl \quad (4)$$

where Cl'_i indicates an Cl^- interstitial defect. The energies of these "solution" reactions can be evaluated by combining appropriate defect energies from simulation methods and lattice energy values.

Calculated solution energies are presented in Figure 2 and three main features emerge. First, Mg^{2+} doping on the Li site is

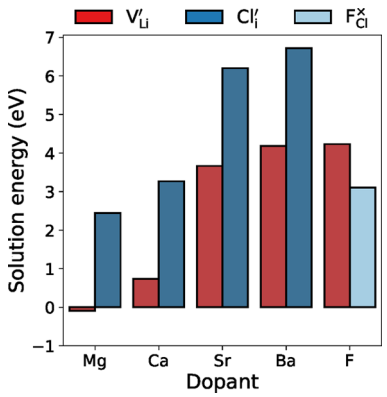

Figure 2. Dopant solution energies for M^{2+} doping and F^- doping in antiperovskite Li_3OCl. Both V'_{Li} (eq 1) and Cl'_i (eq 3) are considered as charge-compensation mechanisms for M^{2+} doping, while V'_{Li} (eq 2) compensated and isovalent $F^{\times}_{Cl}$ doping (eq 4) are considered for F^- doping.

the most energetically favorable dopant, whereas larger ions are far less soluble; this indicates that Mg doping would show the highest solubility and be the most effective in creating mobile Li vacancies. These trends may be related to the similarity in the ionic size between dopants and the substituted host ion, consistent with dopant substitution in ion-conducting perovskite oxides.[52−54]

Second, M^{2+} doping on Li^+ sites with charge compensation via Cl^- interstitial defects is relatively unfavorable, suggesting that such interstitial defects are highly unlikely in the close-packed antiperovskite structure; indeed, anion interstitials have not been observed experimentally in the much studied $BaMO_3$ and $LaMO_3$ perovskite ionic conductors.[54] We note that solution energies derived using dopant oxides as reference states are also presented in Figure S1, which yielded similar trends to the dopant chlorides (eq 1) but slightly higher solution energies for the favorable Mg dopant.

Third, for F-doping, the isovalent mechanism (eq 4) is more energetically favorable than the reaction involving lithium vacancy compensation. As vacant lithium sites are key to improving lithium ion conductivity in Li_3OCl, there may be

https://doi.org/10.1021/acsaem.1c00656
ACS Appl. Energy Mater. XXXX, XXX, XXX−XXX

motivation to overcome this by nonstoichiometric synthesis routes should it significantly improve Li-ion conductivity.

In addition to divalent cations, we note that Al^{3+} was considered as a potential dopant at the Li site with bothLi-vacancy and O-interstitial compensation. However, large calculated energies for both solution modes (8.89 eV for eq 1 and 11.38 eV for eq 3) indicate unfavorable incorporation. This result suggests that Al^{3+} doping may not be the main reason for the enhanced Li-ion conductivity observed in early studies on this material.[19,33]

Turning now to ion transport, molecular dynamics (MD) simulation techniques allow us to investigate the Li-ion conduction properties as a function of charge-carrier concentration and temperature. We use large-scale MD calculations of both undoped and doped Li_3OCl at a range of lithium vacancy concentrations; we stress that our simulations and diffusion statistics using large supercells (>17,000 ions) and long timescales (10 ns) are orders of magnitude greater than that currently attainable by ab initio MD. Mg and F dopants are considered as the most energetically favorable dopants. A low level of cation vacancies (via LiCl Schottky defects) are introduced in the undoped system to facilitate lithium mobility.

Figure 3 shows an Arrhenius plot of the temperature-dependant lithium-ion conductivity for each system. The

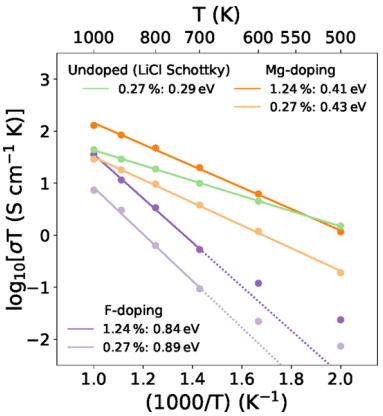

Figure 3. Temperature-dependent Li^+ conductivities (σT) and activation energies (E_a) for F- and Mg-doped Li_3OCl at two lithium vacancy concentrations compared to a low concentration in the undoped system. Solid lines indicate the data from which migration barriers were calculated. Dashed lines indicate extrapolated conductivities in the F-doped system, where Li mobility decreases significantly at lower temperatures.

undoped system shows a conductivity of 3.0×10^{-3} S cm^{-1} at 500 K, which is in good agreement with experimental impedance spectroscopy measurements (2.7×10^{-3} S cm^{-1}).[19]

Mg-doping leads to a slight decrease in ionic conductivity, with an activation barrier of 0.41 eV, which is in good agreement with experimental studies (0.46 eV).[43] However, this is offset by the far higher Li-vacancy concentrations achievable by doping than that occuring in undoped Li_3OCl. The conductivity of the F-doped systems is approximately 2 orders of magnitude lower than undoped Li_3OCl at 700 K, with significantly increased migration barriers in the F-doped system (0.89 eV), both of which are key properties for electrolyte performance. At lower temperatures, Li mobility is insufficient to accurately calculate activation barriers over the timescale studied, so these temperatures were excluded from the fitting.

Dopant−Vacancy Association in Doped Li_3OCl. It is well established that charged point defects can associate to form localized clusters, which can have significant effects on transport behavior.[54,55] An analysis of the ion dynamics and timescale over which these defect clusters form on the atomic scale has not yet been considered for doped Li_3OCl, and often, detailed experimental characterization of such defect clusters can be difficult. Our simulation methods can model the electrostatic, polarization, and elastic strain energies, which are the predominant terms in any local defect association process.

Energy minimization calculations were performed to determine the binding energies of dopant−vacancy pairs in Li_3OCl. Figure 1b−d show the configurations of dopant−vacancy clusters for F^- and M^{2+} doping, along with the Li/Cl vacancy pair (LiCl Schottky), which facilitates lithium mobility in the undoped system.[56] At the dilute limit, binding energies can be calculated by

$$E_{\text{bind}} = E_{\text{cluster}} - \sum_{i=1}^{N} E^{i}_{\text{dilute}} \quad (5)$$

where E_{bind} is the binding energy, E_{cluster} is the energy of the defect pair cluster, and E_{dilute} is the energy of an isolated component of the N defect cluster components at the dilute limit. At higher concentrations, all inequivalent configurations of a Li_3OCl supercell at a given size are relaxed, with a binding energy given by

$$E_{\text{bind}} = E_{\text{cluster}} - \max(E_{\text{configs}}) \quad (6)$$

where E_{configs} is the energies of all unique configurations.

Figure 4 shows the calculated binding energies of dopant−vacancy pairs with three main features that can be identified.

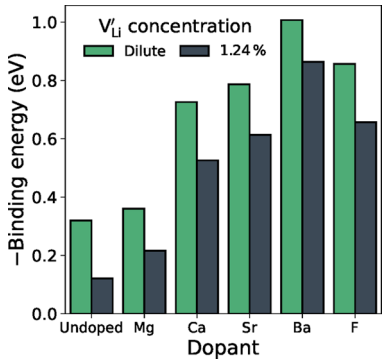

Figure 4. Defect binding energies for M^{2+} (eq 1) and F^- (eq 2) dopants in Li_3OCl for two lithium vacancy concentrations.

First, Mg^{2+} has the smallest vacancy binding energies for cation doping. At the dilute limit, Li vacancies are loosely bound to Mg dopants, with only slightly higher binding energies than the undoped system. This indicates that dopant−vacancy interactions will not significantly reduce the lithium ion mobility of Mg-doped Li_3OCl. The similarity between the ionic radii of Mg and Li (0.72 and 0.76 Å, respectively)[57] limits local lattice distortion. Larger degrees of local lattice distortion is known to result in increased elastic or polarization effects that increase the interactions between the dopant and vacancy, thereby explaining the comparatively high binding energies calculated for larger M^{2+} dopant ions, as found in previous studies.[50−53]

https://doi.org/10.1021/acsaem.1c00656
ACS Appl. Energy Mater. XXXX, XXX, XXX−XXX

Second, the highest dopant−vacancy binding energies are found at the dilute limit, with binding energies decreasing for the 1.24% dopant concentration. This is attributed to dopant−vacancy−dopant interactions, with vacancies in a pair being attracted to other nearby dopants, offsetting the binding energy of the isolated cluster. Previous DFT studies on this system predict that M^{2+} doping in Li_3OCl forms dopant−vacancy pair clusters at low temperatures[43,44] but did not consider higher dopant concentrations or high temperatures.

Third, all other M^{2+} dopants and F^- doping on the O site show high binding energies (>0.5 eV), which would significantly hinder lithium mobility in these materials, reducing their viability as solid electrolytes. The high binding energies for F-doping on the O site likely arises due to the smaller Li−O interatomic distances (1.96 Å) than the separations of both Li−Li and Li−Cl (2.77 Å each). The relatively low solution and binding energies of Mg^{2+} dopants as compared to F^- doping may also be of relevance to the hydrated $Li_2(OH)Cl$ system, where F-doping has been shown to enhance ionic conductivity.[31] These results suggest clustering of F dopant ions and Li vacancies (rather than a random distribution) as possible precursors to larger clusters or nanodomains, which we then examine using the MD simulation data.

Figure 5 shows the distribution of lithium vacancies in three different structures at two temperatures: undoped, Mg-doped,

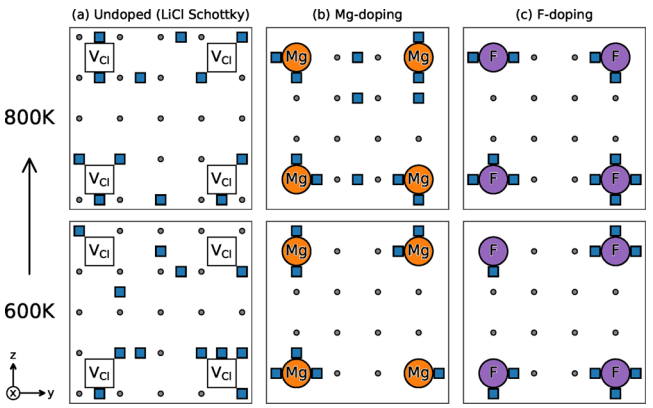

Figure 5. Snapshots of MD simulations viewed along [100] (~60 Å depth), demonstrating defect clustering effects at 600 and 800 K (t = 150 ps), using Wigner−Seitz cell analysis: (a) undoped, (b) Mg-doped, and (c) F-doped. 1.24% of lithium sites are vacant, indicated by blue squares. Cl vacancies are shown with hollow squares, Mg dopants with orange circles, F dopants with purple circles, and O sites with small gray circles. Occupied Li and Cl sites have been omitted for clarity.

and F-doped systems. A high distribution of free vacancies indicates that the binding energies are small relative to the average kinetic energy of lithium ions at a given temperature, while dopant−vacancy clusters indicate that the binding energy is sufficient to inhibit long-range lithium-ion mobility. The presence of these dopant clusters within the short simulation timescale indicates that defect clustering is a favorable and rapid process.

In the undoped system, lithium vacancies are widely distributed at 600 K, indicating that the binding energy is insufficient to significantly inhibit lithium mobility at this temperature. We note that LiCl Schottky defects are not expected to form at these concentrations but are considered here to allow direct comparison. In contrast, the majority of lithium vacancies are adjacent to a dopant site in both the Mg- and F-doped systems at 600 K. At 800 K, lithium vacancies are found to dissociate more frequently from Mg dopant ions, while the remaining bound to F sites. The significant differences in Li-ion conductivity found between systems can be rationalized by Li vacancy trapping effects, preventing long-range lithium mobility in systems with higher binding energies. One of the aims of this work is to encourage further structural study to probe such defect clustering at the local level.

CONCLUSIONS

An understanding of the mechanisms that both enhance and inhibit lithium-ion conductivity is vital if next-generation solid electrolytes are to be realized. In this study, we have gained quantitative and atomistic details on the modes of dopant incorporation, the dopant−vacancy binding energies, and the Li-ion transport properties of F- and Mg-doped Li_3OCl. Three key conclusions can be drawn. First, the most favorable doping mechanism is Mg incorporation with Li vacancy compensation, which would facilitate Li-ion conductivity. Second, the increase in Li vacancy concentration and lower dopant−vacancy binding energy for Mg-doping provides a means of improving the electrochemical performance of Li_3OCl. Third, high binding energies between F-dopants and lithium vacancies lead to defect clustering and significantly higher Li-ion migration barriers, inhibiting long-range Li-ion migration in accordance with the observed decrease in Li-ion conductivity in F-doped Li_3OCl. The lack of long-range Li-ion transport can be rationalized by considering the trapping of Li vacancies.

The tuning of vital solid electrolyte properties, such as Li-ion conductivity and electrochemical stability, via extrinsic doping is essential to achieve state-of-the-art solid-state batteries. The atomistic insights described in this work illustrate the importance of considering the binding between dopants and Li-ion charge-carriers since it can potentially eclipse the anticipated benefit of having a high charge-carrier concentration.

METHODS

Atomistic simulation methods based on effective interatomic potentials are widely used and have been described more thoroughly elsewhere.[54,55] Previous studies on solid electrolyte materials including undoped Li_3OCl have successfully applied these techniques to yield both structural and ion transport properties.[37,41,58−62] Such atomistic techniques have the advantage of examining defect and ionic conduction processes at much larger length scales and timescales than electronic structure methods.

Short-range ion interactions are modeled using Buckingham-type interatomic potentials, while long-range interactions are modeled using Coulombic terms. Energy minimization calculations account for local polarization effects via the shell model, allowing the displacement of ion shells from their cores subject to a harmonic potential.[63] Interatomic potential parameters are given in the Supporting Information (Tables S1 and S2). Defect energies at dilute concentrations are calculated using the Mott−Littleton approximation,[64] implemented in the General Utility Lattice Program (GULP).[65]

The LAMMPS[66] code was used for all MD calculations. Long timescale simulations of 10 ns were performed with a time step of 1 fs, with supercells containing around 17,000−20,000 ions, to ensure confidence in the calculated conductivities and activation barriers. Lithium vacancies are initially distributed randomly, while positive defects (Cl vacancy, Mg dopant, and F dopant) are distributed in a symmetric arrangement to maximize their ion−ion spacing.

https://doi.org/10.1021/acsaem.1c00656
ACS Appl. Energy Mater. XXXX, XXX, XXX−XXX

Simulations were carried out over a temperature range of 500 to 1000 K in intervals of 100 K in the *NPT* ensemble using a Nosé−Hoover thermostat.[67] Conductivities were derived from the mean-squared displacement (MSD) of lithium ions and calculated using the Nernst−Einstein equation, with a Haven ratio of 1, as in previous studies.[30,37,41,58] The tracking of individual vacancies utilizes Wigner−Seitz cell analysis, comparing doped and thermally distorted systems at a given time step to a pristine reference lattice.[68,69]

■ ASSOCIATED CONTENT

Supporting Information

The Supporting Information is available free of charge at https://pubs.acs.org/doi/10.1021/acsaem.1c00656.

Interatomic potential parameters, Solution energies derived using dopant oxides as reference states, and Representative MSDs of each species in both undoped and doped Li_3OCl (PDF)

■ AUTHOR INFORMATION

Corresponding Author

M. Saiful Islam − *Department of Chemistry, University of Bath, Bath BA2 7AY, U.K.;* orcid.org/0000-0003-3882-0285; Email: M.S.Islam@bath.ac.uk

Authors

Matt J. Clarke − *Department of Chemistry, University of Bath, Bath BA2 7AY, U.K.;* orcid.org/0000-0003-1371-4160

James A. Dawson − *Chemistry—School of Natural and Environmental Science and Centre for Energy, Newcastle University, Newcastle upon Tyne NE1 7RU, U.K.;* orcid.org/0000-0002-3946-5337

Timothy J. Mays − *Department of Chemical Engineering, University of Bath, Bath BA2 7AY, U.K.;* orcid.org/0000-0003-4468-9869

Complete contact information is available at: https://pubs.acs.org/10.1021/acsaem.1c00656

Notes

The authors declare no competing financial interest.

■ ACKNOWLEDGMENTS

For jointly funding a PhD studentship, the authors thank the EPSRC Centre for Doctoral Training in Sustainable Chemical Technologies (EP/L016354/1) and CFH Docmail Ltd. (Radstock, UK). We are grateful to the Faraday Institution (FIGR003) and UK Materials and Molecular Modelling Hub for computational resources, which is partially funded by EPSRC (EP/P020194/1). J.A.D. also acknowledges Newcastle University for funding through a Newcastle Academic Track (NUAcT) Fellowship.

■ REFERENCES

(1) Campanella, D.; Belanger, D.; Paolella, A. Beyond garnets, phosphates and phosphosulfides solid electrolytes: New ceramic perspectives for all solid lithium metal batteries. *J. Power Sources* **2021**, *482*, 228949.

(2) Zhu, F.; Islam, M. S.; Zhou, L.; Gu, Z.; Liu, T.; Wang, X.; Luo, J.; Nan, C. W.; Mo, Y.; Ma, C. Single-atom-layer traps in a solid electrolyte for lithium batteries. *Nat. Commun.* **2020**, *11*, 1828.

(3) Famprikis, T.; Canepa, P.; Dawson, J. A.; Islam, M. S.; Masquelier, C. Fundamentals of inorganic solid-state electrolytes for batteries. *Nat. Mater.* **2019**, *18*, 1278−1291.

(4) Lin, D.; Liu, Y.; Cui, Y. Reviving the lithium metal anode for high-energy batteries. *Nat. Nanotechnol.* **2017**, *12*, 194−206.

(5) Guo, Y.; Li, H.; Zhai, T. Reviving Lithium-Metal Anodes for Next-Generation High-Energy Batteries. *Adv. Mater.* **2017**, *29*, 1700007.

(6) Gao, Z.; Sun, H.; Fu, L.; Ye, F.; Zhang, Y.; Luo, W.; Huang, Y. Promises, Challenges, and Recent Progress of Inorganic Solid-State Electrolytes for All-Solid-State Lithium Batteries. *Adv. Mater.* **2018**, *30*, 1870122.

(7) Kerman, K.; Luntz, A.; Viswanathan, V.; Chiang, Y.-M.; Chen, Z. Practical Challenges Hindering the Development of Solid State Li Ion Batteries. *J. Electrochem. Soc.* **2017**, *164*, A1731−A1744.

(8) Kim, J.-J.; Yoon, K.; Park, I.; Kang, K. Progress in the Development of Sodium-Ion Solid Electrolytes. *Small Methods* **2017**, *1*, 1700219.

(9) Manthiram, A.; Yu, X.; Wang, S. Lithium battery chemistries enabled by solid-state electrolytes. *Nat. Rev. Mater.* **2017**, *2*, 1−16.

(10) Chen, R.; Qu, W.; Guo, X.; Li, L.; Wu, F. The pursuit of solid-state electrolytes for lithium batteries: From comprehensive insight to emerging horizons. *Mater. Horiz.* **2016**, *3*, 487−516.

(11) Bachman, J. C.; Muy, S.; Grimaud, A.; Chang, H.-H.; Pour, N.; Lux, S. F.; Paschos, O.; Maglia, F.; Lupart, S.; Lamp, P.; Giordano, L.; Shao-Horn, Y. Inorganic Solid-State Electrolytes for Lithium Batteries: Mechanisms and Properties Governing Ion Conduction. *Chem. Rev.* **2016**, *116*, 140−162.

(12) Richards, W. D.; Miara, L. J.; Wang, Y.; Kim, J. C.; Ceder, G. Interface Stability in Solid-State Batteries. *Chem. Mater.* **2016**, *28*, 266−273.

(13) Tikekar, M. D.; Choudhury, S.; Tu, Z.; Archer, L. A. Design principles for electrolytes and interfaces for stable lithium-metal batteries. *Nat. Energy* **2016**, *1*, 16114.

(14) Li, J.; Ma, C.; Chi, M.; Liang, C.; Dudney, N. J. Solid electrolyte: The key for high-voltage lithium batteries. *Adv. Energy Mater.* **2015**, *5*, 1−6. DOI: 10.1002/aenm.201570018

(15) Wang, Y.; Richards, W. D.; Ong, S. P.; Miara, L. J.; Kim, J. C.; Mo, Y.; Ceder, G. Design principles for solid-state lithium superionic conductors. *Nat. Mater.* **2015**, *14*, 1026−1031.

(16) Krauskopf, T.; Richter, F. H.; Zeier, W. G.; Janek, J. Physicochemical Concepts of the Lithium Metal Anode in Solid-State Batteries. *Chem. Rev.* **2020**, *120*, 7745−7794.

(17) Chen, R.; Li, Q.; Yu, X.; Chen, L.; Li, H. Approaching Practically Accessible Solid-State Batteries: Stability Issues Related to Solid Electrolytes and Interfaces. *Chem. Rev.* **2020**, *120*, 6820−6877.

(18) Zhang, Z.; Shao, Y.; Lotsch, B.; Hu, Y.-S.; Li, H.; Janek, J.; Nazar, L. F.; Nan, C.-W.; Maier, J.; Armand, M.; Chen, L. New horizons for inorganic solid state ion conductors. *Energy Environ. Sci.* **2018**, *11*, 1945−1976.

(19) Zhao, Y.; Daemen, L. L. Superionic conductivity in lithium-rich anti-perovskites. *J. Am. Chem. Soc.* **2012**, *134*, 15042−15047.

(20) Dondelinger, M.; Swanson, J.; Nasymov, G.; Jahnke, C.; Qiao, Q.; Wu, J.; Widener, C.; Numan-Al-Mobin, A. M.; Smirnova, A. Electrochemical stability of lithium halide electrolyte with antiperovskite crystal structure. *Electrochim. Acta* **2019**, *306*, 498−505.

(21) Chen, M.-H.; Emly, A.; Van der Ven, A. Anharmonicity and phase stability of antiperovskite Li3OCl. *Phys. Rev. B* **2015**, *91*, 214306.

(22) Lü, X.; Howard, J. W.; Chen, A.; Zhu, J.; Li, S.; Wu, G.; Dowden, P.; Xu, H.; Zhao, Y.; Jia, Q. Antiperovskite Li 3 OCl Superionic Conductor Films for Solid-State Li-Ion Batteries. *Adv. Sci.* **2016**, *3*, 1500359.

(23) Sagotra, A. K.; Errandonea, D.; Cazorla, C. Mechanocaloric effects in superionic thin films from atomistic simulations. *Nat. Commun.* **2017**, *8*, 963.

(24) Mouta, R.; Diniz, E. M.; Paschoal, C. W. A. Li+ interstitials as the charge carriers in superionic lithium-rich anti-perovskites. *J. Mater. Chem. A* **2016**, *4*, 1586−1590.

(25) Wu, M. S.; Xu, B.; Luo, W. W.; Sun, B. Z.; Ouyang, C. Y. Interfacial properties and Li-ion dynamics between Li3OCl solid electrolyte and Li metal anode for all solid state Li metal batteries from first principles study. *Electrochim. Acta* **2020**, *334*, 135622.

(26) Wang, Y.; Zhang, H.; Zhu, J.; Lü, X.; Li, S.; Zou, R.; Zhao, Y. Antiperovskites with Exceptional Functionalities. *Adv. Mater.* **2020**, *32*, 1905007.
(27) Wang, C.; Fu, K.; Kammampata, S. P.; McOwen, D. W.; Samson, A. J.; Zhang, L.; Hitz, G. T.; Nolan, A. M.; Wachsman, E. D.; Mo, Y.; Thangadurai, V.; Hu, L. Garnet-Type Solid-State Electrolytes: Materials, Interfaces, and Batteries. *Chem. Rev.* **2020**, *120*, 4257−4300.
(28) Ahiavi, E.; Dawson, J. A.; Kudu, U.; Courty, M.; Islam, M. S.; Clemens, O.; Masquelier, C.; Famprikis, T. Mechanochemical synthesis and ion transport properties of Na3OX (X = Cl, Br, I and BH4) antiperovskite solid electrolytes. *J. Power Sources* **2020**, *471*, 228489.
(29) Song, A. Y.; Xiao, Y.; Turcheniuk, K.; Upadhya, P.; Ramanujapuram, A.; Benson, J.; Magasinski, A.; Olguin, M.; Meda, L.; Borodin, O.; Yushin, G. Protons Enhance Conductivities in Lithium Halide Hydroxide/Lithium Oxyhalide Solid Electrolytes by Forming Rotating Hydroxy Groups. *Adv. Energy Mater.* **2018**, *8*, 1870014.
(30) Dawson, J. A.; Attari, T. S.; Chen, H.; Emge, S. P.; Johnston, K. E.; Islam, M. S. Elucidating lithium-ion and proton dynamics in anti-perovskite solid electrolytes. *Energy Environ. Sci.* **2018**, *11*, 2993−3002.
(31) Li, Y.; Zhou, W.; Xin, S.; Li, S.; Zhu, J.; Lü, X.; Cui, Z.; Jia, Q.; Zhou, J.; Zhao, Y.; Goodenough, J. B. Fluorine-Doped Antiperovskite Electrolyte for All-Solid-State Lithium-Ion Batteries. *Angew. Chem., Int. Ed.* **2016**, *55*, 9965−9968.
(32) Lu, Z.; Chen, C.; Baiyee, Z. M.; Chen, X.; Niu, C.; Ciucci, F. Defect chemistry and lithium transport in Li3OCl anti-perovskite superionic conductors. *Phys. Chem. Chem. Phys.* **2015**, *17*, 32547−32555.
(33) Lü, X.; Wu, G.; Howard, J. W.; Chen, A.; Zhao, Y.; Daemen, L. L.; Jia, Q. Li-rich anti-perovskite Li3OCl films with enhanced ionic conductivity. *Chem. Commun.* **2014**, *50*, 11520−11522.
(34) Hanghofer, I.; Redhammer, G. J.; Rohde, S.; Hanzu, I.; Senyshyn, A.; Wilkening, H. M. R.; Rettenwander, D. Untangling the Structure and Dynamics of Lithium-Rich Anti-Perovskites Envisaged as Solid Electrolytes for Batteries. *Chem. Mater.* **2018**, *30*, 8134−8144.
(35) Koedtruad, A.; Patino, M. A.; Ichikawa, N.; Kan, D.; Shimakawa, Y. Crystal structures and ionic conductivity in Li2OHX (X = Cl, Br) antiperovskites. *J. Solid State Chem.* **2020**, *286*, 121263.
(36) Song, A. Y.; Turcheniuk, K.; Leisen, J.; Xiao, Y.; Meda, L.; Borodin, O.; Yushin, G. Understanding Li-Ion Dynamics in Lithium Hydroxychloride (Li 2 OHCl) Solid State Electrolyte via Addressing the Role of Protons. *Adv. Energy Mater.* **2020**, *10*, 1903480.
(37) Dawson, J. A.; Canepa, P.; Famprikis, T.; Masquelier, C.; Islam, M. S. Atomic-Scale Influence of Grain Boundaries on Li-Ion Conduction in Solid Electrolytes for All-Solid-State Batteries. *J. Am. Chem. Soc.* **2018**, *140*, 362−368.
(38) Shen, K.; Wang, Y.; Zhang, J.; Zong, Y.; Li, G.; Zhao, C.; Chen, H. Revealing the effect of grain boundary segregation on Li ion transport in polycrystalline anti-perovskite Li3ClO: A phase field study. *Phys. Chem. Chem. Phys.* **2020**, *22*, 3030−3036.
(39) Wu, M.; Xu, B.; Luo, W.; Sun, B.; Shi, J.; Ouyang, C. First-principles study on the structural, electronic, and Li-ion mobility properties of anti-perovskite superionic conductor Li3OCl (1 0 0) surface. *Appl. Surf. Sci.* **2020**, *510*, 145394.
(40) Emly, A.; Kioupakis, E.; Van Der Ven, A. Phase stability and transport mechanisms in antiperovskite Li 3OCl and Li3OBr superionic conductors. *Chem. Mater.* **2013**, *25*, 4663−4670.
(41) Dawson, J. A.; Chen, H.; Islam, M. S. Composition Screening of Lithium- and Sodium-Rich Anti-Perovskites for Fast-Conducting Solid Electrolytes. *J. Phys. Chem. C* **2018**, *122*, 23978−23984.
(42) Braga, M. H.; Stockhausen, V.; Oliveira, J. C.; Ferreira, J. A. The role of defects in Li3ClO solid electrolyte: Calculations and experiments. *Mater. Res. Soc. Symp. Proc.* **2013**, *1526*, 905.
(43) Braga, M. H.; Ferreira, J. A.; Stockhausen, V.; Oliveira, J. E.; El-Azab, A. Novel Li3ClO based glasses with superionic properties for lithium batteries. *J. Mater. Chem. A* **2014**, *2*, 5470−5480.
(44) Stegmaier, S.; Voss, J.; Reuter, K.; Luntz, A. C. Li+ Defects in a Solid-State Li Ion Battery: Theoretical Insights with a Li3OCl Electrolyte. *Chem. Mater.* **2017**, *29*, 4330−4340.
(45) Fang, H.; Jena, P. Sodium Superionic Conductors Based on Clusters. *ACS Appl. Mater. Interfaces* **2018**, *11*, 963−972.
(46) Fang, H.; Wang, S.; Liu, J.; Sun, Q.; Jena, P. Superhalogen-based lithium superionic conductors. *J. Mater. Chem. A* **2017**, *5*, 13373−13381.
(47) Heenen, H. H.; Voss, J.; Scheurer, C.; Reuter, K.; Luntz, A. C. Multi-ion Conduction in Li 3 OCl Glass Electrolytes. *J. Phys. Chem. Lett.* **2019**, *10*, 2264−2269.
(48) Li, P.; Hussain, F.; Cui, P.; Li, Z.; Yang, J. Boosting ionic conductivity in antiperovskite Li3OCl via defect engineering: Interstitial versus vacancy. *Phys. Rev. Mater.* **2019**, *3*, 115402.
(49) Reckeweg, O.; Blaschkowski, B.; Schleid, T. Li5OCl3 and Li3OCl: Two Remarkably Different Lithium Oxide Chlorides. *Z. Anorg. Allg. Chem.* **2012**, *638*, 2081−2086.
(50) Jones, A.; Islam, M. S. Atomic-scale insight into LaFeO3 perovskite: Defect nanoclusters and ion migration. *J. Phys. Chem. C* **2008**, *112*, 4455−4462.
(51) Tealdi, C.; Malavasi, L.; Fisher, C. A. J.; Islam, M. S. Dispropertionation, dopant incorporation, and defect clustering in perovskite-structured NdCoO3. *J. Phys. Chem. B* **2006**, *110*, 5395−5402.
(52) Islam, M. S. Ionic transport in ABO3 perovskite oxides: A computer modelling tour. *J. Mater. Chem.* **2000**, *10*, 1027−1038.
(53) Islam, M. S.; Davies, R. A. Atomistic study of dopant site-selectivity and defect association in the lanthanum gallate perovskite. *J. Mater. Chem.* **2004**, *14*, 86−93.
(54) Islam, M. S.; Fisher, C. A. J. Lithium and sodium battery cathode materials: Computational insights into voltage, diffusion and nanostructural properties. *Chem. Soc. Rev.* **2014**, *43*, 185−204.
(55) Catlow, R.; Sokol, A.; Walsh, A. *Computational Approaches to Energy Materials*, 1st ed.; John Wiley & Sons Ltd.: Oxford, UK, 2013.
(56) Wu, M.; Xu, B.; Lei, X.; Huang, K.; Ouyang, C. Bulk properties and transport mechanisms of a solid state antiperovskite Li-ion conductor Li3OCl: Insights from first principles calculations. *J. Mater. Chem. A* **2018**, *6*, 1150−1160.
(57) Shannon, R. D. Revised effective ionic radii and systematic studies of interatomic distances in halides and chalcogenides. *Acta Crystallogr., Sect. A: Cryst. Phys., Diffr., Theor. Gen. Crystallogr.* **1976**, *32*, 751−767.
(58) Dawson, J. A.; Canepa, P.; Clarke, M. J.; Famprikis, T.; Ghosh, D.; Islam, M. S. Toward Understanding the Different Influences of Grain Boundaries on Ion Transport in Sulfide and Oxide Solid Electrolytes. *Chem. Mater.* **2019**, *31*, 5296−5304.
(59) Deng, Y.; Eames, C.; Fleutot, B.; David, R.; Chotard, J.-N.; Suard, E.; Masquelier, C.; Islam, M. S. Enhancing the Lithium Ion Conductivity in Lithium Superionic Conductor (LISICON) Solid Electrolytes through a Mixed Polyanion Effect. *ACS Appl. Mater. Interfaces* **2017**, *9*, 7050−7058.
(60) Deng, Y.; Eames, C.; Nguyen, L. H. B.; Pecher, O.; Griffith, K. J.; Courty, M.; Fleutot, B.; Chotard, J.-N.; Grey, C. P.; Islam, M. S.; Masquelier, C. Crystal Structures, Local Atomic Environments, and Ion Diffusion Mechanisms of Scandium-Substituted Sodium Superionic Conductor (NASICON) Solid Electrolytes. *Chem. Mater.* **2018**, *30*, 2618−2630.
(61) Symington, A. R.; Purton, J.; Statham, J.; Molinari, M.; Islam, M. S.; Parker, S. C. Quantifying the impact of disorder on Li-ion and Na-ion transport in perovskite titanate solid electrolytes for solid-state batteries. *J. Mater. Chem. A* **2020**, *8*, 19603−19611.
(62) Famprikis, T.; Dawson, J. A.; Fauth, F.; Clemens, O.; Suard, E.; Fleutot, B.; Courty, M.; Chotard, J.-N.; Islam, M. S.; Masquelier, C. A New Superionic Plastic Polymorph of the Na+ Conductor Na3PS4. *ACS Mater. Lett.* **2019**, *1*, 641−646.
(63) Dick, B. G.; Overhauser, A. W. Theory of the Dielectric Constants of Alkali Halide Crystals. *Phys. Rev.* **1958**, *112*, 90−103.

https://doi.org/10.1021/acsaem.1c00656
ACS Appl. Energy Mater. XXXX, XXX, XXX−XXX

(64) Mott, N. F.; Littleton, M. J. Conduction in polar crystals. I. Electrolytic conduction in solid salts. *Trans. Faraday Soc.* **1938**, *34*, 485−499.
(65) Gale, J. D.; Rohl, A. L. The General Utility Lattice Program (GULP). *Mol. Simul.* **2003**, *29*, 291−341.
(66) Plimpton, S. Fast Parallel Algorithms for Short-Range Molecular Dynamics. *J. Comput. Phys.* **1995**, *117*, 1−19.
(67) Evans, D. J.; Holian, B. L. The Nose−Hoover thermostat. *J. Chem. Phys.* **1985**, *83*, 4069−4074.
(68) Wigner, E.; Seitz, F. On the Constitution of Metallic Sodium. *Phys. Rev.* **1933**, *43*, 804−810.
(69) Stukowski, A. Visualization and analysis of atomistic simulation data with OVITO-the Open Visualization Tool. *Modell. Simul. Mater. Sci. Eng.* **2010**, *18*, 015012.

https://doi.org/10.1021/acsaem.1c00656
ACS Appl. Energy Mater. XXXX, XXX, XXX−XXX